THE DOMAIN DECOMPOSITION METHOD FOR MAXWELL'S EQUATIONS IN TIME DOMAIN SIMULATIONS WITH DISPERSIVE METALLIC MEDIA*

JONG HYUK PARK† AND JOHN C. STRIKWERDA‡

Abstract. The domain decomposition method based on overlapping grids is developed to solve the two-dimensional Maxwell equations in the time domain. The finite difference schemes for rectangular and polar coordinate systems are presented. Since interpolation plays a crucial role in our method, the Newton and the Fourier interpolation methods are surveyed in detail. The computational studies of the electromagnetic wave propagation in free space and the back-scattering by a perfect electric conducting object of a circular shape are performed to test the accuracy, the convergence, and the efficiency of our method. Moreover, we give a methodology to model dispersive media in time domain simulations by introducing Drude conductivity in the constitutive equations. The problem of light scattering by metallic nanoparticles is solved, and its results show that our algorithm is efficient and reliable in capturing the small scale phenomena.

1. Introduction. One of the main difficulties in the development of reliable tools for computational electromagnetics (CEM) based on conventional algorithms like Yee's method [20, 21] (commonly known as the finite difference time domain method (FDTD)) is the treatment of curved interfaces. Brute force discretization using only a rectangular grid requires excessively small grid sizes to reasonably resolve the curvature of the interface, and this frequently forces the use of large amounts of memory and unreasonably long computation times. Furthermore, numerical artifacts (known as staircasing errors) can be introduced and corrupt the solutions. Other algorithms for CEM are discussed in [3, 4, 7, 12, 15, 20].

Recently, domain decomposition methods (DDMs) [18] based on overlapping (or composite) grids have been successfully applied to CEM problems with complex geometries [6, 8]. Henshaw [8] solved Maxwell's equations as a second-order vector wave equation rather than as a first-order system and developed high-order schemes by discretizing the Laplace operator. The jump (or transmission) condition at the interface of two different constant media are derived using boundary- (or interface-) fitted grids.

In this paper, we suggest a more general method. We solve the two-dimensional Maxwell equations as a first-order system with constitutive equations. By doing this, we separate numerical stability issues from material modeling issues (i.e., stable schemes for Maxwell's equations can be used with various materials by simply

---

†Electrical and Computer Engineering Department, Ulsan National Institute of Science and Technology, 100 Bayyeon-ri Eonyang-eup, Ulju-gun, 689-798 Ulsan Metropolitan City, Korea (jong8jong8@gmail.com).

‡Computer Sciences Department, University of Wisconsin, 1210 West Dayton St., Madison, WI 53706 (strik@cs.wisc.edu).

changing the constitutive equations).

We decompose the original (spatial) domain into subdomains, which are of regular shapes (i.e., rectangles, circles, or annuli) and overlap one another to completely cover the original domain. Here, we place no constraint on the overlapped regions other than that the solutions match at the boundaries (or interfaces). In particular, in an overlapped region, each dependent variable has a representation from each subdomain. The agreement, or lack of agreement, between the different subdomains is an indication of how well the method works. These subdomains are discretized based on structured grids for rectangular and polar coordinate systems. The leapfrog finite difference scheme was used on all grids. We also derive formulas to handle the singularity at the origin in polar coordinate systems.

Since information transition across the overlapped domains is critically dependent on the boundary data, we need accurate interpolation methodologies. We use methods that are accurate enough so that the numerical errors introduced by the interpolations are comparable to the truncation error of the schemes. In two-dimensional cases, time marching covers $\mathcal{O}(N_s^2)$ points whereas interpolation covers $\mathcal{O}(N_s)$ points, where N_s is the number of points along a side of a two-dimensional domain. In three-dimensional cases, it is $\mathcal{O}(N_s^3)$ and $\mathcal{O}(N_s^2)$, respectively. Thus, the overhead for interpolation should be small, especially when one considers using it on problems with complicated geometry.

Even though our method is presented for a specific application in this paper, the basic method can be extended in several ways. Certainly, other boundary conditions can be used. Other modifications might include using different numerical methods, such as pseudospectral, finite element, or finite volume methods, on different domains [6, 8, 16]. Moreover, it is our intention to extend this method to three-dimensional computations because parallel processing is natural to use with domain decomposition. However, we do not discuss issues of the parallel implementation in this paper.

2. Interpolations. The Newton interpolation method for the one-dimensional case can be used to approximate functions with supporting points on a straight line. For the given set of x coordinates $\{x_0, x_1, \ldots, x_d\}$ and the corresponding set of ordered pairs $\{(x_i, f_i)\}$ for $i = 0, 1, \ldots, d$, we can consider a polynomial $P_{1\mathrm{D}}(x)$ such that $P_{1\mathrm{D}}(x_i) = f_i$ for $i = 0, 1, \ldots, d$. The distances between x_i and x_{i+1} need not be equal. Specifically, we define the polynomial of degree d as

$$(2.1) \qquad P_{1\mathrm{D}}(x) = a_0 + a_1(x - x_0) + \cdots + a_d(x - x_0)(x - x_1) \cdots (x - x_{d-1}),$$

where the a_i's are the coefficients of $P_{1\mathrm{D}}(x)$. From the theory of divided differences [5], the coefficients are

$$a_i = f[x_0, x_1, \ldots, x_i],$$

and these can be used to get the interpolated value at $x = x^*$, that is, $f(x^*) \approx P_{1\mathrm{D}}(x^*)$ (see [5]).

This idea can be extended to the two-dimensional case. For the given set of x coordinates $\{x_0, x_1, \ldots, x_d\}$ and y coordinates $\{y_0, y_1, \ldots, y_d\}$, we can consider the corresponding set of ordered triples $\{(x_i, y_j, f_{i,j})\}$ for $i, j = 0, 1, \ldots, d$ and $i + j \leq d$. Thus, the two-dimensional polynomial $P_{2\mathrm{D}}(x, y)$ of degree d such that $P_{2\mathrm{D}}(x_i, y_j) = f_{i,j}$ for $i + j \leq d$ can be defined as

$$\begin{aligned} P_{2\mathrm{D}}(x, y) = {} & a_{0,0} + a_{1,0}(x - x_0) + a_{0,1}(y - y_0) + \cdots \\ & + a_{i,j}(x - x_0) \cdots (x - x_i)(y - y_0) \cdots (y - y_j) + \cdots, \end{aligned}$$

where the $a_{i,j}$'s are the coefficients of $P_{2\mathrm{D}}(x, y)$. So, the coefficients are

$$a_{i,j} = f[x_0, \ldots, x_i][y_0, \ldots, y_j],$$

and we get the interpolated value at $(x, y) = (x^*, y^*)$, that is, $f(x^*, y^*) \approx P_{2\mathrm{D}}(x^*, y^*)$ (see [17]).

We have found that cubic interpolation produces a satisfactory level of accuracy. Quadratic interpolation would be sufficient on accuracy considerations, but we chose cubic interpolation because of the slightly smaller errors found in test runs. The evaluation of the cubic interpolation adds very little extra expense to the computation.

The Fourier method is used for the approximation of functions and derivatives when the functions are periodic. We consider only periodic functions with period 2π. First, for the given set of ϕ coordinates

$$(2.2) \qquad \left\{ \phi_j \mid \phi_j = (\Delta\phi)j, \text{ where } \Delta\phi = \frac{2\pi}{J} \text{ for } j = 0, 1, \ldots, J \right\},$$

where J is an even integer, we can consider the corresponding set of ordered pairs $\{(\phi_j, f_j)\}$ for $j = 0, 1, \ldots, J$, and the periodicity is expressed via $f_0 = f_J$.

The basic identity is that the values of f_j can be expressed as

$$f_j = \sum_{k=0}^{J/2}{}' a_k \sin k\phi_j + b_k \cos k\phi_j,$$

where a_0 and $a_{J/2}$ are 0, and the prime on the summation indicates that the first and last terms (i.e., when $k = 0$ and $k = J/2$) are weighted with a $1/2$.

The Fourier coefficients a_k and b_k are easily obtained by the use of the formulas

$$a_k = \frac{2}{J} \sum_{j=0}^{J-1} f_j \sin k\phi_j, \quad b_k = \frac{2}{J} \sum_{j=0}^{J-1} f_j \cos k\phi_j.$$

Note that there are J nontrivial coefficients a_k and b_k and there are J independent values of f_j. Of course, $a_0 = a_{J/2} = 0$.

Once the coefficients are determined, the 2π-periodic function $f(\phi)$ can be approximated by the formula

$$(2.3) \qquad f(\phi) \approx \sum_{k=0}^{J/2}{}' a_k \sin k\phi + b_k \cos k\phi.$$

Moreover, (2.3) can be used to get approximate values of $df/d\phi$. The formula can be obtained by differentiating (2.3) with respect to ϕ as

$$(2.4) \qquad \frac{df}{d\phi}(\phi) \approx \sum_{k=0}^{J/2}{}' k a_k \cos k\phi - k b_k \sin k\phi.$$

The two-dimensional interpolation of f at a point (ρ^*, ϕ^*) can be done by the combination of (2.3) and (2.1) when the data are on a polar grid. For the given set of ρ coordinates $\{\rho_0, \ldots, \rho_d\}$ and the set of ϕ coordinates as in (2.2), we can consider the set of ordered triples $\{(\rho_i, \phi_j, f_{i,j})\}$ for $i = 0, 1, \ldots, d$ and $j = 0, 1, \ldots, J$ where J is an

even integer, such that $f(\rho_i, \phi_j) = f_{i,j}$. By periodicity, $f_{i,0} = f_{i,J}$ for every value of i. Fourier interpolation depicted in (2.3) allows the approximation of $f(\rho_i, \phi^*) \approx f_i^*$ for $i = 0, 1, \ldots, d$. From this, the set of ordered pairs $\{(\rho_i, f_i^*)\}$ for $i = 0, 1, \ldots, d$ allows us to determine the coefficients of the polynomial as in (2.1), and this polynomial approximates the function $f^*(\rho)$. Therefore, (2.1) gives the approximate values of $f(\rho^*, \phi^*) \approx f^*(\rho^*)$.

3. Maxwell's equations and the constitutive equations. Maxwell's equations in t-space [10] are

$$(3.1) \qquad \frac{\partial \mathbf{B}}{\partial t} + \nabla \times \mathbf{E} = 0, \quad \frac{\partial \mathbf{D}}{\partial t} - \nabla \times \mathbf{H} = -\mathbf{J}, \quad \nabla \cdot \mathbf{B} = 0, \quad \nabla \cdot \mathbf{D} = q_v,$$

where $\mathbf{B}$ is the magnetic induction, $\mathbf{D}$ is the electric displacement, $\mathbf{H}$ is the magnetic field intensity, $\mathbf{E}$ is the electric field intensity, $\mathbf{J} = \mathbf{J}^c + \mathbf{J}^i$ is the total electric current density, $\mathbf{J}^c$ is the conduction electric current density, $\mathbf{J}^i$ is the impressed electric current density, and q_v is the volume charge density. We assume that $q_v = 0$ in this paper.

For a scalar function $f(t)$ defined on $t \geq 0$, we define the Fourier transform as

$$\mathfrak{F}\{f(t)\} \equiv \frac{1}{\sqrt{2\pi}} \int_{-\infty}^{\infty} f(t)\, e^{-i\omega t}\, dt = \hat{f}(\omega)$$

and its inverse transform as

$$\mathfrak{F}^{-1}\left\{\hat{f}(\omega)\right\} \equiv \frac{1}{\sqrt{2\pi}} \int_{-\infty}^{\infty} \hat{f}(\omega)\, e^{i\omega t}\, d\omega = f(t).$$

The convolution operator $*$ for two functions $f(t)$ and $g(t)$ is defined as

$$(f * g)(t) = \int_0^t f(t - t')g(t')\, dt' = \mathfrak{F}^{-1}\left\{\hat{f}(\omega)\hat{g}(\omega)\right\}.$$

Maxwell's equations in ω-space can be easily obtained using the Fourier transform.

The constitutive equations for isotropic and linear dispersive media are

$$\mathbf{B} = \mu * \mathbf{H}, \quad \mathbf{D} = \epsilon * \mathbf{E}, \quad \mathbf{J}^c = \sigma * \mathbf{E},$$

where $\mu \equiv \mu(t)$ is the permeability function, $\epsilon \equiv \epsilon(t)$ is the permittivity function, and $\sigma \equiv \sigma(t)$ is the electric conductivity function. Since the convolution on t reflects the influence of the time-history, it is used to define constitutive equations that describe the historical interaction of the fields with dispersive material properties.

For example, the permittivity function of free space can be modeled as $\epsilon(t) = \epsilon_0\delta(t)$, where $\epsilon_0 \approx 8.8541878 \times 10^{-12}$ (F/m) is the permittivity in free space and $\delta(t)$ is the Dirac-delta function (i.e., instantaneous response). In this case,

$$\mathbf{D} = \epsilon * \mathbf{E} = \int_0^t \epsilon_0\delta(t - t')\mathbf{E}(t', \mathbf{r})\, dt' = \epsilon_0\mathbf{E}.$$

Similarly, with $\mu(t) = \mu_0\delta(t)$, we have $\mathbf{B} = \mu_0\mathbf{H}$ for free space, where $\mu_0 = 4\pi \times 10^{-7} \approx 1.2566370 \times 10^{-6}$ (H/m) is the permeability in free space. Notice that the Dirac-delta function $\delta(t)$ has a physical unit of inverse time (s^{-1}).

When all fields are independent of the variable z (the variable for a rectangular or a cylindrical coordinate system), Maxwell's equations decouple into two systems

JONG HYUK PARK AND JOHN C. STRIKWERDA

of equations—the TM_z equations and the TE_z equations in two-dimensional space. The TM_z equations in a rectangular coordinate system are

$$(3.2a) \qquad \frac{\partial B_x}{\partial t} + \frac{\partial E_z}{\partial y} = 0,$$

$$(3.2b) \qquad \frac{\partial B_y}{\partial t} - \frac{\partial E_z}{\partial x} = 0,$$

$$(3.2c) \qquad \frac{\partial D_z}{\partial t} - \frac{\partial H_y}{\partial x} + \frac{\partial H_x}{\partial y} = -J_z^c - J_z^i$$

and in a polar coordinate system are

$$(3.3a) \qquad \frac{\partial B_\rho}{\partial t} + \frac{1}{\rho}\frac{\partial E_z}{\partial \phi} = 0,$$

$$(3.3b) \qquad \frac{\partial B_\phi}{\partial t} - \frac{\partial E_z}{\partial \rho} = 0,$$

$$(3.3c) \qquad \frac{\partial D_z}{\partial t} - \frac{1}{\rho}\frac{\partial \rho H_\phi}{\partial \rho} + \frac{1}{\rho}\frac{\partial H_\rho}{\partial \phi} = -J_z^c - J_z^i.$$

Likewise, the TE_z equations in a rectangular coordinate system are

$$(3.4a) \qquad \frac{\partial D_x}{\partial t} - \frac{\partial H_z}{\partial y} = -J_x^c - J_x^i,$$

$$(3.4b) \qquad \frac{\partial D_y}{\partial t} + \frac{\partial H_z}{\partial x} = -J_y^c - J_y^i,$$

$$(3.4c) \qquad \frac{\partial B_z}{\partial t} + \frac{\partial E_y}{\partial x} - \frac{\partial E_x}{\partial y} = 0$$

and in a polar coordinate system are

$$(3.5a) \qquad \frac{\partial D_\rho}{\partial t} - \frac{1}{\rho}\frac{\partial H_z}{\partial \phi} = -J_\rho^c - J_\rho^i,$$

$$(3.5b) \qquad \frac{\partial D_\phi}{\partial t} + \frac{\partial H_z}{\partial \rho} = -J_\phi^c - J_\phi^i,$$

$$(3.5c) \qquad \frac{\partial B_z}{\partial t} + \frac{1}{\rho}\frac{\partial \rho E_\phi}{\partial \rho} - \frac{1}{\rho}\frac{\partial E_\rho}{\partial \phi} = 0.$$

4. The finite difference schemes. We use the notation $f|_{i,j}^{n}$ for the grid function approximating a function $f(t,x,y) = f(n\Delta t, i\Delta x, j\Delta y)$ in a rectangular coordinate system or $f(t,\rho,\phi) = f(n\Delta t, i\Delta\rho, j\Delta\phi)$ in a polar coordinate system. We give the leapfrog schemes only for the TM_z equations, but the leapfrog schemes for the TE_z equations or various other schemes for these equations can be easily derived [19].

The leapfrog schemes for the TM_z equations (3.2) in a rectangular coordinate system are

$$(4.1a) \qquad B_x|_{i,j}^{n} = B_x|_{i,j}^{n-2} - \frac{\Delta t}{\Delta y}\left[E_z|_{i,j+1}^{n-1} - E_z|_{i,j-1}^{n-1} \right],$$

$$(4.1b) \qquad B_y|_{i,j}^{n} = B_y|_{i,j}^{n-2} + \frac{\Delta t}{\Delta x}\left[E_z|_{i+1,j}^{n-1} - E_z|_{i-1,j}^{n-1} \right],$$

$$
\begin{aligned}
(4.1c) \qquad D_z|_{i,j}^{n} = {} & D_z|_{i,j}^{n-2} + \frac{\Delta t}{\Delta x}\left[H_y|_{i+1,j}^{n-1} - H_y|_{i-1,j}^{n-1} \right] \\
& - \frac{\Delta t}{\Delta y}\left[H_x|_{i,j+1}^{n-1} - H_x|_{i,j-1}^{n-1} \right] \\
& - 2\Delta t\, J_z^c|_{i,j}^{n-1} - 2\Delta t\, J_3^i|_{i,j}^{n-1}.
\end{aligned}
$$

Next, we consider the finite difference schemes for the TM_z equations in polar coordinate systems. For notational simplicity, let $\rho_i \equiv i\Delta\rho$. First, we give the scheme at the origin. Then, we give the scheme for the grid points adjacent to the origin and the scheme for the remaining points.

Since (3.3a) and (3.3c) are singular at the origin (i.e., $\rho = 0$), we need formulas for the origin. Note that the singularity is due to the coordinate system and not the equations themselves. First, applying l'Hôpital's rule to the second term of (3.3a) gives

$$\lim_{\rho\to 0} \frac{\frac{\partial E_z}{\partial\phi}(t,\rho,\phi)}{\rho} = \frac{\partial^2 E_z}{\partial\rho\partial\phi}(t,0,\phi);$$

the formula of (3.3a) at the origin can be derived as

$$(4.2) \qquad \left[\frac{\partial B_\rho}{\partial t} + \frac{\partial^2 E_z}{\partial\rho\partial\phi} \right](t,0,\phi) = 0.$$

This formula can be used to develop a finite difference scheme at the origin.

The derivation of the scheme for (3.3c) at the origin needs special care to properly accommodate a point source. The main idea is to regard the D_z value at the origin as the average value over a disk of radius $\Delta\rho/2$ centered at the origin. A point source is considered at the origin via $J_z^i = f_p(t)\delta_p(\rho)$ in (3.3c), where $f_p(t)$ is the time profile and $\delta_p(\rho)$ is the *two-dimensional* Dirac-delta distribution in a polar coordinate system that satisfies the following condition:

$$(4.3) \qquad \int\!\!\int_{\Omega_j} \delta_p(\rho)\,\rho\,d\rho\,d\phi = \begin{cases} 1 & \text{if the origin is in the domain,} \\ 0 & \text{otherwise.} \end{cases}$$

By integrating (3.3c) over a disc of radius ρ_d and taking the limit as ρ_d tends to 0, we obtain

$$(4.4) \qquad \lim_{\rho \to 0} \int_0^{2\pi} \rho H_\phi(t, \rho, \phi) d\phi = f_p(t).$$

It should be noted that H_ϕ is *not* finite at the origin if $f_p(t) \neq 0$. If the pointwise limit of ρH_ϕ is the same for each value of ϕ, then (4.4) can be represented as

$$(4.5) \qquad \lim_{\rho \to 0} \rho H_\phi(t, \rho, \phi) = \frac{1}{2\pi} f_p(t).$$

If we define an average operator as

$$\frac{1}{\pi(\Delta\rho/2)^2} \int_0^{\Delta\rho/2} \int_0^{2\pi} [\cdot]\, \rho\, d\rho\, d\phi$$

and apply this average to (3.3c), the following formula can be obtained:

$$(4.6) \qquad \begin{aligned} \frac{\partial D_z}{\partial t}(t,0,0) &= \frac{1}{\pi(\rho_{1/2})^2} \int_0^{2\pi} \rho_{1/2} H_\phi(t, \rho_{1/2}, \phi)\, d\phi \\ &\quad - \frac{1}{\pi(\rho_{1/2})^2} \int_0^{\rho_{1/2}} \int_0^{2\pi} J_z^c(t,\rho,\phi)\, \rho\, d\rho\, d\phi - \frac{1}{\pi(\rho_{1/2})^2} f_p(t). \end{aligned}$$

To approximate the first integral in (4.6), the value of ρH_ϕ at $\rho_{1/2}$ is replaced by its average of the values at ρ_1 and ρ_0 (here, the relation in (4.4) is used for the value at ρ_0), resulting in the following approximation:

$$\int_0^{2\pi} \rho_{1/2} H_\phi(t, \rho_{1/2}, \phi)\, d\phi \approx \frac{1}{2} \int_0^{2\pi} \rho_1 H_\phi(t, \rho_1, \phi)\, d\phi + \frac{1}{2} f_p(t).$$

The second integral in (4.6) can be approximated as

$$\int_0^{\rho_{1/2}} \int_0^{2\pi} J_z^c(t,\rho,\phi)\, \rho\, d\rho\, d\phi \approx \frac{1}{4} \int_0^{\rho_1} \int_0^{2\pi} J_z^c(t,\rho,\phi)\, \rho\, d\rho\, d\phi.$$

So, the formula of (3.3c) at the origin is given as

$$(4.7) \qquad \begin{aligned} \frac{\partial D_z}{\partial t}(t,0,0) &= \frac{2}{\pi(\Delta\rho)^2} \int_0^{2\pi} \Delta\rho H_\phi(t, \Delta\rho, \phi)\, d\phi \\ &\quad - \frac{1}{\pi(\Delta\rho)^2} \int_0^{\Delta\rho} \int_0^{2\pi} J_z^c(t,\rho,\phi)\, \rho\, d\rho\, d\phi - \frac{2}{\pi(\Delta\rho)^2} f_p(t). \end{aligned}$$

We approximate the integrals in this equation with the trapezoid rule.

Therefore, with the formulas (4.2), (3.3b), and (4.7), the leapfrog scheme at the origin is

$$(4.8a) \qquad B_\rho|_{0,j}^n = B_\rho|_{0,j}^{n-2} - \frac{\Delta t}{\Delta\rho}\left[\left.\frac{\partial E_z}{\partial \phi}\right|_{1,j}^{n-1} - \left.\frac{\partial E_z}{\partial \phi}\right|_{1,j^*}^{n-1} \right],$$

$$(4.8b) \qquad B_\phi|_{0,j}^n = B_\phi|_{0,j}^{n-2} + \frac{\Delta t}{\Delta\rho}\left[E_z|_{1,j}^{n-1} - E_z|_{1,j^*}^{n-1} \right],$$

$$D_z|_{0,j}^n = D_z|_{0,j}^{n-2} + \frac{8\Delta t}{\Delta\rho J} \sum_{j=0}^{J-1} H_\phi|_{1,j}^{n-1}$$

(4.8c)

$$- \frac{4\Delta t\Delta\rho}{J} \sum_{j=0}^{J-1} J_z^c|_{1,j}^{n-1} - \frac{4\Delta t}{\pi(\Delta\rho)^2} \; f_p|^{n-1},$$

where $j^* = (j+J/2)\%J$ for the total sampling number J in the ϕ axis with the modulo operator %. Angular derivatives are approximated using Fourier interpolation as in (2.4) at each time step.

At $\rho_i = \rho_1 = \Delta\rho$ (i.e., $i = 1$), the leapfrog scheme for (3.3a), (3.3b), and (3.3c) is

(4.9a)
$$B_\rho|_{1,j}^n = B_\rho|_{1,j}^{n-2} - \frac{2\Delta t}{\rho_1} \left.\frac{\partial E_z}{\partial\phi}\right|_{1,j}^{n-1},$$

(4.9b)
$$B_\phi|_{1,j}^n = B_z|_{1,j}^{n-2} + \frac{\Delta t}{\Delta\rho} \left[E_z|_{2,j}^{n-1} - E_z|_{0,j}^{n-1} \right],$$

(4.9c)
$$D_z|_{1,j}^n = D_z|_{1,j}^{n-2} + \frac{\Delta t}{\rho_1\Delta\rho} \left[\rho_2 \, H_\phi|_{2,j}^{n-1} - \frac{1}{2\pi} \, f_p|^{n-1} \right]$$
$$- \frac{2\Delta t}{\rho_1} \left.\frac{\partial H_\rho}{\partial\phi}\right|_{1,j}^{n-1} - 2\Delta t \, J_3^c|_{1,j}^{n-1} - 2\Delta t \, J_3^i|_{1,j}^{n-1}.$$

At $\rho_i \geq 2\Delta\rho$ (i.e., $i \geq 2$), the leapfrog scheme for (3.3) of the TM_z equations in a polar coordinate system is

(4.10a)
$$B_\rho|_{i,j}^n = B_\rho|_{i,j}^{n-2} - \frac{2\Delta t}{\rho_i} \left.\frac{\partial E_z}{\partial\phi}\right|_{i,j}^{n-1},$$

(4.10b)
$$B_\phi|_{i,j}^n = B_\phi|_{i,j}^{n-2} + \frac{\Delta t}{\Delta\rho} \left[E_z|_{i+1,j}^{n-1} - E_z|_{i-1,j}^{n-1} \right],$$

(4.10c)
$$D_z|_{i,j}^n = D_z|_{i,j}^{n-2} + \frac{\Delta t}{\rho_i\Delta\rho} \left[\rho_{i+1} \, H_\phi|_{i+1,j}^{n-1} - \rho_{i-1} \, H_\phi|_{i-1,j}^{n-1} \right]$$
$$- \frac{2\Delta t}{\rho_i} \left.\frac{\partial H_\rho}{\partial\phi}\right|_{i,j}^{n-1} - 2\Delta t \, J_z^c|_{i,j}^{n-1} - 2\Delta t \, J_z^i|_{i,j}^{n-1}.$$

5. The choice of parameters for computations. In this paper, we conjecture that the Courant–Friedrichs–Lewy (CFL) stability condition has the form

$$\Delta t < \frac{C_{st}}{c\sqrt{(\frac{1}{\Delta_1})^2 + (\frac{1}{\Delta_2})^2}},$$

where C_{st} is a constant and c is the (maximum) speed of propagation.

The CFL condition of the leapfrog scheme on a rectangular gird is

$$\Delta t < \frac{C_{rec}}{c\sqrt{(\frac{1}{\Delta x})^2 + (\frac{1}{\Delta y})^2}},$$

where $C_{rec} = 1$. This condition can be verified for a single hyperbolic equation [19], and it is satisfactory for Maxwell's equations as well. We can use this CFL condition to determine the size of a time step for the required spatial resolution.

The CFL condition of the leapfrog schemes applied to the domain of an annulus whose ρ spans in $\rho_{min} \leq \rho \leq \rho_{max}$ is assumed to be

$$\Delta t < \frac{C_{ann}}{c\sqrt{(\frac{1}{\Delta\rho})^2 + (\frac{1}{\rho_{min}\Delta\phi})^2}},$$

where $C_{ann} \approx 0.3$ has been determined by numerical experiment.

The CFL condition of the leapfrog schemes applied to the domain of a circle of radius ρ_{max} is assumed to be

$$\Delta t < \frac{C_{cir}}{c\sqrt{(\frac{1}{\Delta\rho})^2 + (\frac{1}{\Delta\rho\Delta\phi})^2}},$$

where $C_{cir} \approx 0.3$ has been determined by numerical experiment.

The time step that is the smallest over all of the domains is chosen as the one time step for the algorithm. The leapfrog scheme is von Neumann stable under this CFL condition. With interpolation there can be weak instability, as has been shown by Olsson and Petersson [13]. In our computations, we did, however, notice small instabilities in the vicinity of the corners of our computational domain. To remove this, we added fourth-order dissipation [19]. We used the magnitude of the dissipation parameter $\varepsilon = 0.005$.

With this dissipation we did not see anything that might be termed an instability due to the interpolation between domains. Our computations were over thousands of time steps, and so there was ample opportunity for any instability to show itself.

We have found that the sampling number for the angular direction (N_ϕ) such that $\Delta\phi = 2\pi/N_\phi$ for an annulus or a circle should be chosen by the rule

(5.1) $$N_\phi \geq 12 \left(\frac{\rho_{max}}{\rho_{unit}}\right),$$

where $\rho_{unit} = 1$. This has worked well in our numerical simulations.

6. The overview of the time-marching algorithm. For the time-marching algorithm, we regard the DDM as a collection of initial boundary value problems (IBVPs)—one IBVP for each subdomain. The solutions in the interior are advanced in parallel at each time step. The boundary data along a boundary introduced by the overlapping procedure come from solutions in the interior of other domains. The data must be supplied using boundary conditions that are well-posed for IBVPs.

These boundary conditions are not classical continuity conditions because there are no physical interfaces at the overlapped boundaries. At an arbitrary point in space where there is physical continuity, the *continuity* conditions are that everything is continuous. However, to supply too much data along the overlapped boundary of a subdomain or to supply it in an ill-posed manner will lead to instability. This instability is not the result of the domain decomposition but is a standard instability due to improper boundary conditions for an IBVP.

Because Maxwell's equations are hyperbolic, not all components of the solution can be specified along a boundary and have a well-posed problem. If the Poynting

vector $\mathbf{S}_{\mathrm{bc}} = \mathbf{E}_{\mathrm{bc}} \times \mathbf{H}_{\mathrm{bc}} = c^2(\mathbf{D}_{\mathrm{bc}} \times \mathbf{B}_{\mathrm{bc}})$ is tangential at the point on a boundary, $\mathbf{E}_{\mathrm{bc}}$ and $\mathbf{H}_{\mathrm{bc}}$ (or $\mathbf{D}_{\mathrm{bc}}$ and $\mathbf{B}_{\mathrm{bc}}$) are the field components that can be specified.

This is a well-posed boundary condition for Maxwell's partial differential equations. These boundary conditions hold not only along the boundary of the total region but also along the introduced boundaries of each domain. For an introduced domain, these components are determined by taking values from the same physical point in an overlapping domain. In this way, each domain has a well-posed IBVP. The domains are coupled in that the specified boundary values on the introduced boundary of one domain are equal to interior values of another domain.

The numerical algorithm requires that all components must be determined on the boundary. The boundary conditions required by the partial differential equations determine some of the components but not all. The others must be determined by extrapolation from inside the computational domain; see Strikwerda [19]. This separates the components of the solution, along a boundary, into the set that is specified in one way or another from data external to the domain and the set that is determined from internal data.

7. Electromagnetic wave propagation in free space. In this section, we solve the TM_z equations (3.2) with a point source in free space (i.e., $J_z^c = 0$, $\mu = \mu_0$, and $\epsilon = \epsilon_0$). The original square domain $\overline{\Omega} = \{(x,y) \mid (x,y) \in [-5,5] \times [-5,5]\}$ is given as in Figure 7.1(a). At the origin $(0,0) \in \overline{\Omega}$, the point source

$$(7.1) \qquad J_z^i(t,x,y) = f_p(t)\delta(x - x_s, y - y_s)$$

with the smooth function proposed by Kriegsmann, Norris, and Reiss [11],

$$(7.2) \qquad f_p(t) = \begin{cases} \frac{1}{32}\left[10 - 15\cos\omega t + 6\cos 2\omega t - \cos 3\omega t\right] & \text{for } 0 \le t \le T_p, \\ 0 & \text{for } t > T_p, \end{cases}$$

is considered, where $T_p = 2\pi/\omega$. In this problem, the D_z-fields at $t = 4$ on the line $\{(x,y) \mid x \in [0.1,5], y = 0\} \subset \overline{\Omega}$ are computed using our method, and their accuracies are tested since the exact solutions for this problem are known. In the tests, all the initial conditions are zero and the propagation speed is normalized (i.e., $c = 1$). The point source in (7.1) with the time profile in (7.2) (where $\omega = 0.5\pi$) is used.

First, $\overline{\Omega}$ is decomposed into six subdomains $\overline{\Omega}_j$, which are specified as (see Figure 7.1)

$$\begin{aligned} \overline{\Omega}_0 &= \{(\rho,\phi) \mid (\rho,\phi) \in [0,3] \times [0,2\pi]\}, \\ \overline{\Omega}_1 &= \{(\rho,\phi) \mid (\rho,\phi) \in [2,4] \times [0,2\pi]\}, \\ \overline{\Omega}_2 &= \{(x,y) \mid (x,y) \in [-5,5] \times [-5,-2]\}, \\ \overline{\Omega}_3 &= \{(x,y) \mid (x,y) \in [-5,-2] \times [-5,5]\}, \\ \overline{\Omega}_4 &= \{(x,y) \mid (x,y) \in [2,5] \times [-5,5]\}, \\ \overline{\Omega}_5 &= \{(x,y) \mid (x,y) \in [-5,5] \times [2,5]\}. \end{aligned}$$

We discretize these subdomains with the same sizes of all the spatial grids (i.e., $\Delta x = \Delta y = \Delta\rho = \Delta$). We test the cases when $(\Delta, N_\phi(\overline{\Omega}_0), N_\phi(\overline{\Omega}_1)) = (1/10, 12, 24)$, $(1/20, 24, 36)$, and $(1/40, 36, 48)$. The errors are essentially independent of direction, and we choose to display only the errors along the line $\phi = 0$ as these display the effects of the interpolation in the overlap regions. It must be noted that the observation line passes $\overline{\Omega}_0$, $\overline{\Omega}_1$, and $\overline{\Omega}_4$, including their overlapped regions. The errors are measured
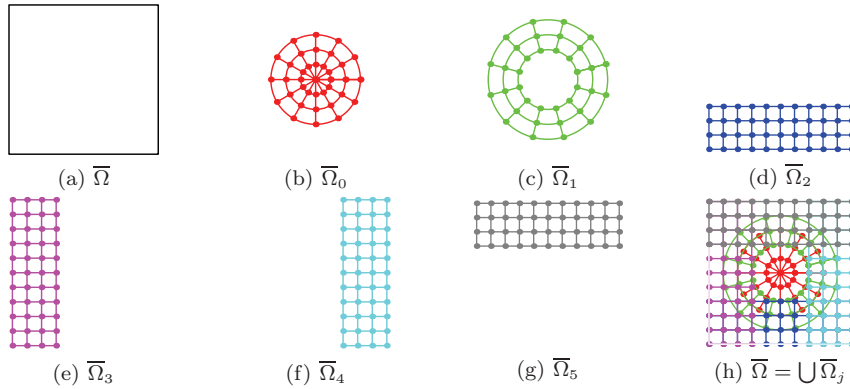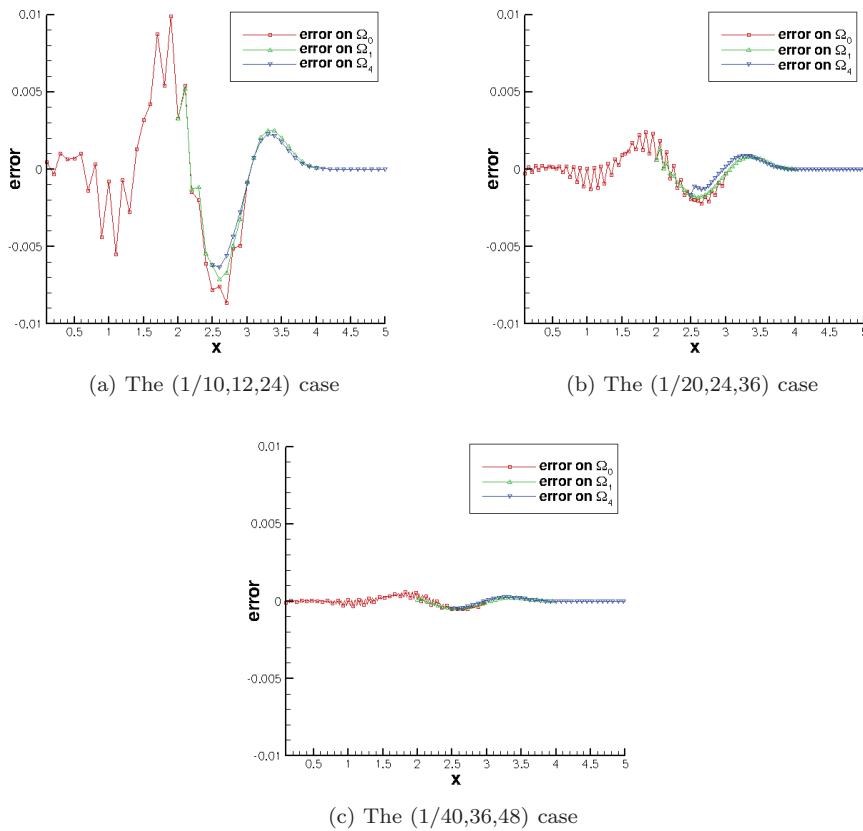
(a) $\overline{\Omega}$ (b) $\overline{\Omega}_0$ (c) $\overline{\Omega}_1$ (d) $\overline{\Omega}_2$

(e) $\overline{\Omega}_3$ (f) $\overline{\Omega}_4$ (g) $\overline{\Omega}_5$ (h) $\overline{\Omega} = \bigcup \overline{\Omega}_j$

FIG. 7.1. *Domain decomposition process.*

(a) The (1/10,12,24) case

(b) The (1/20,24,36) case

(c) The (1/40,36,48) case

FIG. 7.2. *The accuracy of DDM computation (TM_z equations).*

for these subdomains, respectively, and Figure 7.2 gives the results. For each case, the max-errors are 0.00987, 0.00241, and 0.00060, respectively. We can observe that our method conserves second-order accuracy.

In testing the method we found that the accuracy was acceptable if the subdomains overlap by a minimum of five grid points. Note that using cubic interpolation

requires at least a three-point overlap since all the interpolation points must be interior points. The values at boundary points are themselves determined from interpolation and so are not available for interpolation to other boundaries.

For overlaps smaller than five points, the errors were larger, but the method was not unstable. We consider the five-point overlap restriction, rather than the minimal three-point, to be a small cost to pay for the simplicity of the overall algorithm and the gain in accuracy.

8. Further grid refinement tests. In this section, we solve the TM_z equations (3.2) with a perfect electric conducting (PEC) object of a circular shape (see Figure 8.1) in free space. An exact solution expressed in ω-space for this problem is available. However, we focus on testing transient (or time-dependent) back-scattering phenomena in this section.

In the original square domain $\overline{\Omega} = \{(x,y) \mid (x,y) \in [-7,7] \times [-7,7]\}$, as in Figure 8.1, the center of the circular PEC object $\overline{\Omega}_{\mathrm{PEC}} = \{(\rho,\phi) \mid (\rho,\phi) \in [0,2] \times [0,2\pi]\}$ is located at $(0,1) \in \overline{\Omega}$. The PEC object is realized by setting D_z- and B_ρ-fields to zero on the inner boundary of $\overline{\Omega}_0$. B_ϕ-fields are computed using a numerical boundary condition (e.g., the backward-time backward-space scheme). The same point source as in section 7 is located at $(0,-1.5) \in \overline{\Omega}$. In this problem, we want to measure the back-scattered D_z-fields at $t = 4$ on the line $\{(x,y) \mid x \in [-2.5,2.5], y = -3.5\} \subset \overline{\Omega}$. The reflections are very angle-dependent and show the performance of PEC implementations.

To test the convergence of our method, we decompose $\overline{\Omega}$ into five subdomains $\overline{\Omega}_j$, which are specified as (see Figure 8.2(a))

$$\begin{aligned}
\overline{\Omega}_0 &= \{(\rho,\phi) \mid (\rho,\phi) \in [2,4] \times [0,2\pi]\}, \\
\overline{\Omega}_1 &= \{(x,y) \mid (x,y) \in [-7,7] \times [-7,-3]\}, \\
\overline{\Omega}_2 &= \{(x,y) \mid (x,y) \in [-7,7] \times [4,7]\}, \\
\overline{\Omega}_3 &= \{(x,y) \mid (x,y) \in [-7,-2.5] \times [-3,5]\}, \\
\overline{\Omega}_4 &= \{(x,y) \mid (x,y) \in [-2.5,7] \times [-3,5]\},
\end{aligned}$$

where the center of the annular subdomain $\overline{\Omega}_0$ is located at $(0,1) \in \overline{\Omega}$.

We discretize these subdomains with the grid sizes $\Delta x = \Delta y = \Delta \rho = \Delta$ and $\Delta \phi = 2\pi/N_\phi$. In Figure 8.3(a), we test for the cases when $(\Delta, N_\phi) = (1/10,\ 12)$, $(1/10,\ 24)$, $(1/10,\ 36)$, $(1/10,\ 48)$, $(1/10,\ 60)$, and $(1/10,\ 72)$. This shows that we need at least $N_\phi \geq 48$ to adequately resolve the reflection (see (5.1)). In Figure 8.3(b), we compare the cases when $(\Delta, N_\phi) = (1/10,\ 48)$, $(1/20,\ 48)$, and $(1/40,\ 48)$. Figures 8.3(a) and 8.3(b) indicate that N_ϕ is a critical factor in the modeling of a circular PEC object.

To test the influence of grid refinements, we solve the same problem but using a rectangular grid with grid sizes $\Delta x = \Delta y = \Delta_{\mathrm{rec}} = 1/100,\ 1/200$, and $1/400$, respectively. We mimic the circular PEC object (i.e., the cylinder) with rectangular PEC patches (see Figure 8.2(b)) where B_y- and D_z-fields are specified with zero for the grid points within or on the PEC object. B_x-fields are computed using the backward-time forward-space scheme as a numerical boundary condition (a similar PEC implementation for Yee's algorithm can be found in [9]). These results are compared with the case in Figure 8.2(a) where $(\Delta, N_\phi) = (1/20,\ 48)$ (see Figure 8.4). The values of the two runs agree well near $x = 0$ for straight back-reflection but differ significantly for larger angles of reflection. This would be due to the inaccuracy of reflections from the stair step approximation of the cylinder, and it seems to be
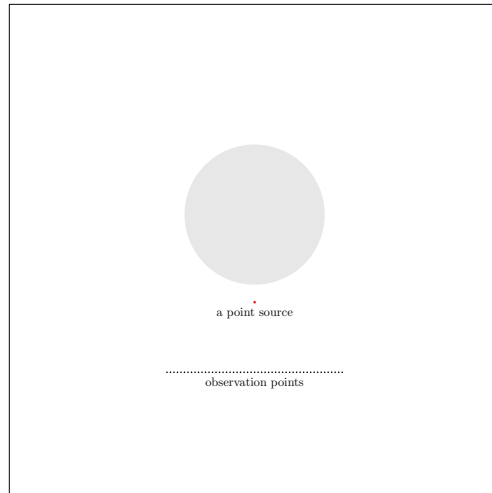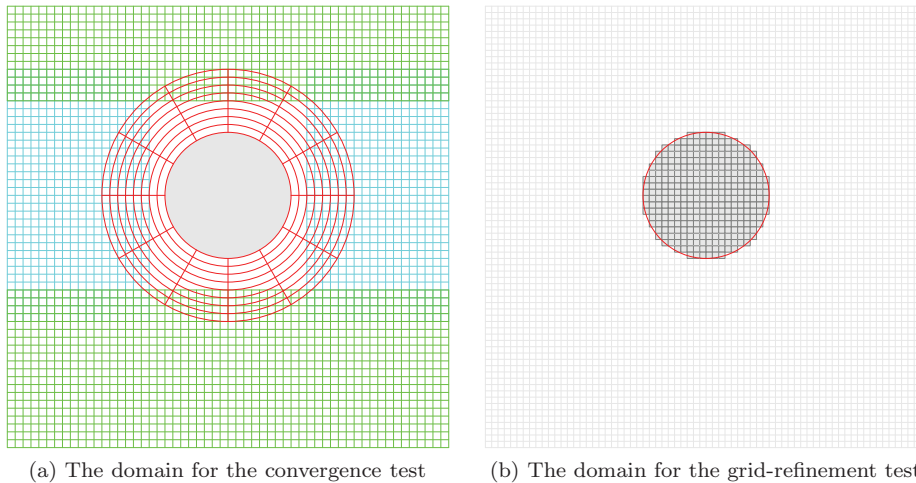
FIG. 8.1. *A circular PEC object with a point source.*

(a) The domain for the convergence test   (b) The domain for the grid-refinement test

FIG. 8.2. *The PEC back-scattering simulation.*

persistent even for finer resolutions. A similar study revealing the inaccuracies for oblique electromagnetic interfaces is done in [9] for Yee's algorithm. Holland [9] suggests a conformal mesh approach as a remedy. The persistence of the inaccuracy from the stair step approximation is not too surprising and highlights the need for methods such as the DDM that treat the boundaries accurately.

A 2.5 GHz Intel Core Duo machine with 4 GB RAM computed the case when $(\Delta, N_\phi) = (1/20, 48)$ in 121 seconds for the time step $\Delta_t = 0.01$. The case when $\Delta_{\text{rec}} = 1/100$ took 625 seconds for the time step $\Delta_t = 0.005$, the case when $\Delta_{\text{rec}} = 1/200$ took 6,218 seconds for the time step $\Delta_t = 0.0025$, and the case when $\Delta_{\text{rec}} = 1/400$ took 67,832 seconds for the time step $\Delta_t = 0.00125$. Although, for similar sized grids, the single rectangular grid is computed much faster than the DDM, the quality of the answer is poorer than the DDM. To get comparable accuracy, the DDM is significantly more efficient.
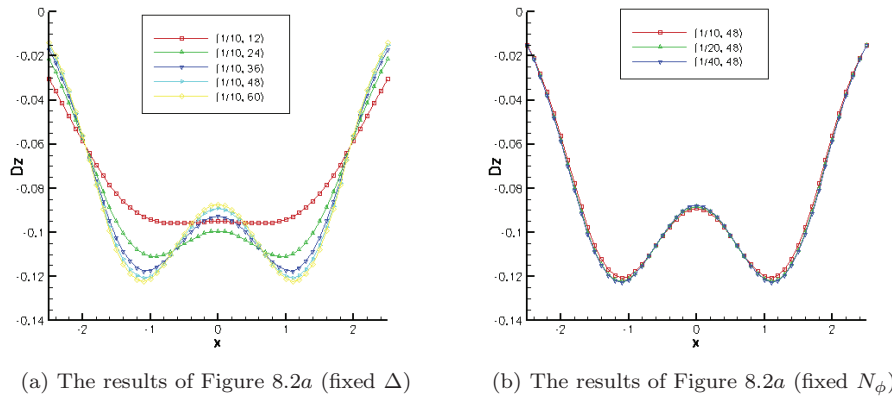
(a) The results of Figure 8.2a (fixed Δ)   (b) The results of Figure 8.2a (fixed N_ϕ)
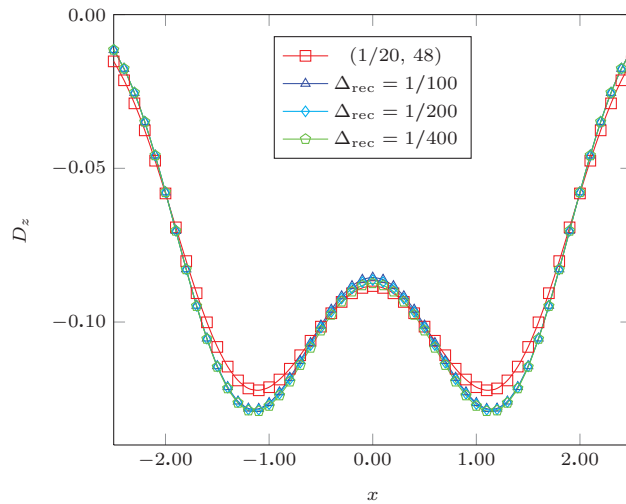
FIG. 8.3. *The convergence test.*

FIG. 8.4. *The grid-refinement test.*

9. The Drude model via the constitutive equations. Generally, conductivities are material functions that indicate collective free electron flows, and permittivities are the material functions that indicate collective polarization of bound electrons (i.e., the collective effect of dipoles caused by extremely small displacements of bound electrons). Since they are theoretically related to each other [10], it is common to measure only permittivities [14] by experiments to determine them in ω-space and use their t-space expressions in time domain simulations [7, 20].

In particular, the model suggested by Drude (in 1900) has been widely used for metallic media. We realize the Drude model via the constitutive equations in this paper—not via the continuity equation as in [7], nor via the auxiliary equations as in [20]. However, our methodology gives reasonable results, as the others do.

The semiclassical equation of the motion of a free electron under the applied **E**-field is

$$(9.1) \qquad m^* \frac{\partial^2 \mathbf{r}}{\partial t^2} + \frac{m^*}{\tau} \frac{\partial \mathbf{r}}{\partial t} = -e\mathbf{E},$$

where $\mathbf{r}$ is the displacement, m^* is the effective mass of the electron, τ is the relaxation time, and e is the electronic charge (i.e., $e = 1.602 \times 10^{-19}$ (C)) [22]. The electric polarization $\hat{\mathbf{P}}$ for n electrons in a unit volume is

$$\hat{\mathbf{P}} \equiv (-e)n\hat{\mathbf{r}} = \frac{ne^2\tau/m^*}{(i\omega)(1 + i\omega\tau)}\hat{\mathbf{E}},$$

where $\hat{\mathbf{r}}$ is the ω-space expression of $\mathbf{r}$ from (9.1). The electric displacement $\hat{\mathbf{D}}$ is

$$\hat{\mathbf{D}} \equiv \hat{\epsilon}_D\hat{\mathbf{E}} = \epsilon_0\epsilon_{r,\infty}\hat{\mathbf{E}} + \hat{\mathbf{P}},$$

where $\epsilon_{r,\infty}$ is the interband-transition contribution to the dielectric constant [22]. So, the Drude permittivity $\hat{\epsilon}_D$ is

$$(9.2) \qquad \hat{\epsilon}_D = \epsilon_0 \left[\epsilon_{r,\infty} - \frac{\omega_p^2}{\omega(\omega - i/\tau)} \right],$$

where $\omega_p = \sqrt{(ne^2)/(\epsilon_0 m^*)}$ is the plasma frequency. Its t-space expression is

$$(9.3) \qquad \epsilon_D = \epsilon_0 \left[\epsilon_{r,\infty}\delta(t) + \omega_p^2\tau \left(1 - e^{-t/\tau} \right) \right].$$

The constants $\epsilon_{r,\infty}$, ω_p, and τ (i.e., they are all positive real numbers) are determined based on experimental data [14, 22].

Here, caution must be used because the term $\omega_p^2/\omega(\omega - i/\tau)$ in (9.2) is singular at $\omega = 0$. Furthermore, (9.1) allows unbounded solutions (i.e., the infinite displacement $\mathbf{r} = \infty$). Therefore, instead of the conventional methods that use $\hat{\mathbf{D}} = \hat{\epsilon}_D\hat{\mathbf{E}}$ and $\hat{\mathbf{J}}^c = 0$, we use $\hat{\mathbf{D}} = \epsilon_0\epsilon_{r,\infty}\hat{\mathbf{E}}$ and $\hat{\mathbf{J}}^c = \hat{\sigma}_D\hat{\mathbf{E}}$ (or their t-space expressions), introducing Drude conductivity $\hat{\sigma}_D$.

With the velocity of the electron $\mathbf{v} = \partial\mathbf{r}/\partial t$ for (9.1) and its ω-space expression $\hat{\mathbf{v}}$, the conduction current $\hat{\mathbf{J}}^c$ is

$$(9.4) \qquad \hat{\mathbf{J}}^c \equiv (-e)n\hat{\mathbf{v}} = \left(\frac{ne^2\tau/m^*}{1 + i\omega\tau} \right) \hat{\mathbf{E}} = \left(\frac{\sigma_{\mathrm{DC}}}{1 + i\omega\tau} \right) \hat{\mathbf{E}} = \hat{\sigma}_D \hat{\mathbf{E}},$$

where $\hat{\sigma}_D(\omega) = \sigma_{\mathrm{DC}}/(1 + i\omega\tau)$ is known as the Drude conductivity. Notice that $\sigma_{\mathrm{DC}} = ne^2\tau/m^* = \hat{\sigma}_D(0)$. Thus, the t-space expression of (9.4) is

$$(9.5) \qquad \mathbf{J}^c = (-e)n\mathbf{v} = (\sigma_D * \mathbf{E}) = \frac{\sigma_{\mathrm{DC}}}{\tau} \int_0^t e^{-(t-t')/\tau} \mathbf{E}(t') \, dt',$$

where the t-space expression of $\hat{\sigma}_D(\omega)$ is

$$(9.6) \qquad \sigma_D(t) = \frac{\sigma_{\mathrm{DC}}}{\tau}e^{-t/\tau}.$$

Of course, $\hat{\sigma}_D$ is perfectly characterized by experimental data (i.e., $\sigma_{\mathrm{DC}} = \epsilon_0 \omega_p^2 \tau$ and τ determine $\hat{\sigma}_D$).

One might use (A8) in [7], which is

$$\frac{\partial\mathbf{J}^c}{\partial t} + \frac{\mathbf{J}^c}{\tau} = \omega_p^2\epsilon_0\mathbf{E},$$

instead of (9.5) to derive a finite difference scheme. Gray and Kupka [7] arrive at a similar approach using this equation to solve for $\mathbf{J}^c$.

10. The finite difference schemes for metallic media. For the constant $\mu = \mu_0$ and the constant $\epsilon = \epsilon_0\epsilon_{r,\infty}$, the constitutive equations become

$$\mathbf{B} = \mu * \mathbf{H} = \mu_0\mathbf{H}, \quad \mathbf{D} = \epsilon * \mathbf{E} = \epsilon_0\epsilon_{r,\infty}\mathbf{E}.$$

Hence,

$$\mathbf{H}|_{i,j}^n = \frac{1}{\mu_0} \left.\mathbf{B}\right|_{i,j}^n, \quad \mathbf{E}|_{i,j}^n = \frac{1}{\epsilon_0\epsilon_{r,\infty}} \left.\mathbf{D}\right|_{i,j}^n.$$

These are very straightforward and easy to implement. However, $\sigma(t)$ in (9.6) and its convolution with the **E**-field need to be explained step by step in the development of their finite difference schemes.

We rewrite the convolution with the Drude conductivity $\sigma_D(t)$ in (9.6) as

$$(10.1) \qquad \mathbf{J}^c(t) = \int_0^t \sigma_D(t - t') \, \mathbf{E}(t') \, dt' = \frac{\sigma_{\mathrm{DC}}}{\tau} \int_0^t e^{-(t-t')/\tau} \, \mathbf{E}(t') \, dt',$$

and we use (10.1) for $t + \Delta t$ to get the following formula:

$$(10.2) \qquad \mathbf{J}^c(t + \Delta t) = e^{-\Delta t/\tau} \, \mathbf{J}^c(t) + \frac{\sigma_{\mathrm{DC}}}{\tau} \, e^{-\Delta t/\tau} \int_t^{t+\Delta t} e^{-(t-t')/\tau} \, \mathbf{E}(t') \, dt'.$$

If we use the trapezoidal rule [5], which is

$$\int_t^{t+\Delta t} f(t') \, dt' \approx \frac{\Delta t}{2} \left[f(t) + f(t + \Delta t) \right],$$

to approximate the last integral in (10.2), then we get the following formula:

$$\mathbf{J}^c(t + \Delta t) \approx e^{-\Delta t/\tau} \, \mathbf{J}^c(t) + \frac{\sigma_{\mathrm{DC}}\Delta t}{2\tau} \left[e^{-\Delta t/\tau}\mathbf{E}(t) + \mathbf{E}(t + \Delta t) \right].$$

Therefore, we obtain the following finite difference scheme for metal modeling:

$$(10.3) \qquad \mathbf{J}^c|_{i,j}^{n-1} = e^{-\Delta t/\tau} \, \mathbf{J}^c|_{i,j}^{n-2} + \frac{\sigma_{\mathrm{DC}}\Delta t}{2\tau} \left[e^{-\Delta t/\tau} \, \mathbf{E}|_{i,j}^{n-2} + \mathbf{E}|_{i,j}^{n-1} \right].$$

Since this determination of $\mathbf{J}^c$ is essentially an evaluation of the integral in (10.1), it does not affect the stability of the overall scheme. Because the scheme and the trapezoid method are both second-order accurate, the overall accuracy is maintained.

11. Electromagnetic wave scattering by metallic nanoparticles. Various geometrical arrays of metallic nanoparticles have been used to investigate controlling light below its diffraction limits [7]. We demonstrate that our DDM method can be applied to the simulations of light scattering by silver (Ag) nanoparticles. We solve the TE_z equations in rectangular (3.2) and in polar (3.3) coordinate systems and the constitutive equations for the dispersive metallic media.

Recently, the scattering of light (i.e., the electromagnetic waves) by metallic nanoparticles has been investigated because geometrical structures composed of these particles can be used to control light below its diffraction limits [2, 7, 20].

In this section, the light scattering phenomena by a funnel array of silver (Ag) nanoparticles (i.e., $\epsilon_{r,\infty} = 3.7$, $\omega_p = 1.38 \times 10^{16}$ Hz, and $\tau = 3.6 \times 10^{-16}$ s) as in Figure 11.1(a) (where $\theta = 45°$, $a = 40$ nm, $b = 25$ nm, and $c = 25$ nm) are simulated.

(a) The original nanodisk arrays   (b) The domain decomposition
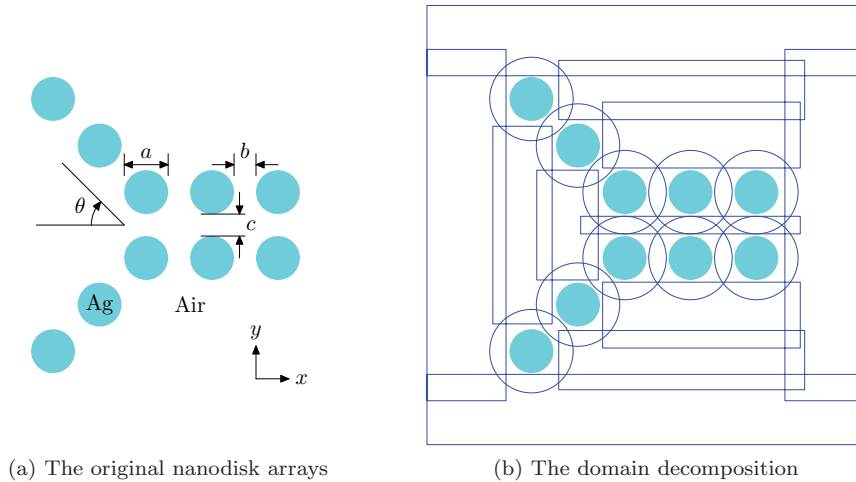
FIG. 11.1. *The funnel nanodisk arrays.*

Since metallic nanoparticles are usually represented by nanodisks in two dimensions, we use ten circular domains for them to have the grids fitted to the boundaries, and the rest of the area is covered with eleven rectangular domains (see Figure 11.1(b)). For the grids of these decomposed domains, we have taken the size of spatial grids as $\Delta x = \Delta y = 1.25$ nm, and $\Delta \rho = 1.25$ nm and $\Delta \phi = 2\pi/36$ for the rectangular and circular domains, respectively, with the time step $\Delta t = 1.333 \times 10^{-19}$ s. In addition, a Kriegsmann function (7.2) of $T_p = 3.333$ fs is used as the time profile of a normally incident H_z-polarized planewave from the left edge of the original domain.

Figure 11.2 displays time snapshots of $|\mathbf{E}| = \sqrt{E_x^2 + E_y^2}$ for the funnel array in Figure 11.1(a). In multiply covered regions, results from all the domains are displayed. The color maps in Figure 11.2 span 0.0 to $2.0 \times \sqrt{\mu_0/\epsilon_0} \times 10^{-7}$, but, for notational simplicity, we drop $\sqrt{\mu_0/\epsilon_0} \times 10^{-7}$. No numerical effects from the decomposed domains are noticeable in the results, and no inconsistencies exist between fields in the overlapped regions. These snapshots demonstrate the complicated interaction of $\mathbf{E}$-fields with the Ag nanoparticle array revealing a strong confinement of $|\mathbf{E}|$.

When the Ag nanoparticles are exposed to the normally incident planewave, they begin to reveal their circular contour as in Figure 11.2(c). In Figure 11.2(c), the portion of the impinging planewave that is normal to the circular boundaries of the revealed two particles is reflected back after little penetration (i.e., a skin depth [10]), and this can be observed as small dots on the two particles, respectively. The other portions that are not normal begin to encircle the particles, and this can be recognized by the yellowish color around the particles. As the incident planewave propagates further, it reveals more particles, and the complicated interaction with the particles can be seen in Figure 11.2(d). When the planewave reaches the inlet of the funnel array as in Figure 11.2(e), we observe the strong confinement of the fields, but it begins to fade, leaving its traces on the particles it has passed (see Figures 11.2(e) and 11.2(f)). Unfortunately, the experimental realization of this funnel array has not been done elsewhere to our knowledge, but the computational results in [7] are very similar to ours.
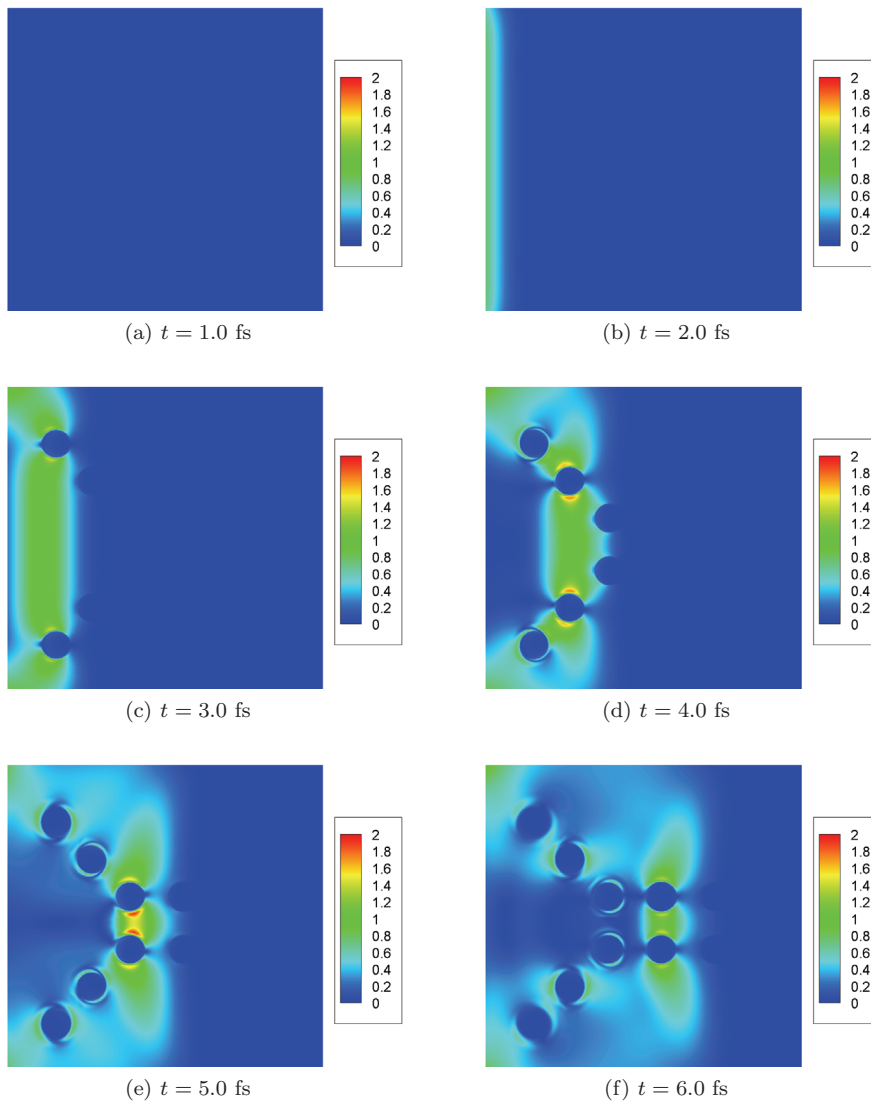
(a) $t = 1.0$ fs   (b) $t = 2.0$ fs

(c) $t = 3.0$ fs   (d) $t = 4.0$ fs

(e) $t = 5.0$ fs   (f) $t = 6.0$ fs

FIG. 11.2. *The scattering patterns of the funnel nanodisk arrays.*

12. Conclusions. In this paper, we have presented an algorithm based on overlapping domain decomposition methods for Maxwell's equations. The finite difference schemes for Maxwell's equations for rectangular and polar coordinate systems have been presented, and interpolation methods have been explained as well. The Drude model is realized via the constitutive equations to model dispersive metallic media in time domain simulations. We have applied it in the simulations of scattering phenomena by metallic nanoparticles. The computational results confirm that our DDM method excellently captures the small scale phenomena.

REFERENCES

[1] N. W. Ashcroft and N. D. Mermin, *Solid State Physics*, Thomson Learning, Boston, MA, 1976.

[2] W. L. Barnes, A. Dereux, and T. W. Ebbesen, *Surface plasmon subwavelength optics*, Nature, 424 (2003), pp. 824–830.

[3] E. J. Bond, X. Li, S. C. Hagness, and B. D. Van Veen, *Microwave imaging via space-time beamforming for early detection of breast cancer*, IEEE Trans. Antennas and Propagation, 51 (2003), pp. 1690–1705.

[4] N. Chavannes, R. Tay, N. Nikoloski, and N. Kuster, *Suitability of FDTD-based TCAD tools for RF design of mobile phones*, IEEE Trans. Antennas Propagat. Mag., 45 (2003), pp. 52–66.

[5] S. D. Conte and C. de Boor, *Elementary Numerical Analysis: An Algorithmic Approach*, 3rd ed., McGraw–Hill, New York, 1980.

[6] T. A. Driscoll and B. Fornberg, *Block pseudospectral methods for Maxwell's equations II: Two-dimensional, discontinuous-coefficient case*, SIAM J. Sci. Comput., 21 (1999), pp. 1146–1167.

[7] S. K. Gray and T. Kupka, *Propagation of light in metallic nanowire arrays: Finite-difference time-domain studies of silver cylinders*, Phys. Rev. B., 68 (2003), 0454515.

[8] W. D. Henshaw, *A high-order accurate parallel solver for Maxwell's equations on overlapping grids*, SIAM J. Sci. Comput., 28 (2006), pp. 1730–1765.

[9] R. J. Holland, *Pitfalls of staircase meshing*, IEEE Trans. Electromagnetic Compatibility, 35 (1993), pp. 434–439.

[10] J. D. Jackson, *Classical Electrodynamics*, John Wiley & Sons, New York, 1999.

[11] G. A. Kriegsmann, A. N. Norris, and E. L. Reiss, *Acoustic pulse scattering by baffled membranes*, J. Acoustic Soc. Amer., 79 (1986), pp. 1–8.

[12] S. Noda, A. Chutinan, and M. Imapa, *Trapping and emission of photons by a single defect in a photonic bandgap structure*, Nature, 407 (2000), pp. 608–610.

[13] F. Olsson and N. A. Petersson, *Stability of interpolation on overlapping grids*, Comput. & Fluids, 25 (1996), pp. 583–605.

[14] E. D. Palik, *Handbook of Optical Constants of Solids*, 2nd ed., Academic Press, Orlando, FL, 1997.

[15] M. J. Piket-May, A. Taflove, and J. Baron, *FDTD modeling of digital signal propagation in 3D circuits with passive and active loads*, IEEE Trans. Microwave Theory Tech., 42 (1994), pp. 1514–1523.

[16] A. Quarteroni, *Domain decomposition methods for systems of conservation laws: Spectral collocation approximations*, SIAM J. Sci. Statist. Comput., 11 (1990), pp. 1029–1052.

[17] I. Rugene and K. H. Bishop, *Analysis of Numerical Methods*, John Wiley & Sons, Indianapolis, IN, 1966.

[18] B. F. Smith, P. E. Bjørstad, and W. D. Gropp, *Domain Decomposition: Parallel Multilevel Methods for Elliptic Partial Differential Equations*, Cambridge University Press, New York, 1996.

[19] J. C. Strikwerda, *Finite Difference Schemes and Partial Differential Equations*, 2nd ed., SIAM, Philadelphia, 2004.

[20] A. Taflove and S. C. Hagness, *Computational Electrodynamics: The Finite-Difference Time-Domain Method*, 3rd ed., Artec House, Norwood, MA, 2005.

[21] K. Yee, *Numerical solution of initial boundary value problems involving Maxwell's equations in isotropic media*, IEEE Trans. Antennas and Propagation, 14 (1966), pp. 302–307.

[22] P. Y. Yu and M. Cardona, *Fundamentals of Semiconductors: Physics and Material Properties*, 3rd ed., Springer, New York, 2001.

[23] E. Zauderer, *Partial Differential Equations of Applied Mathematics*, 2nd ed., John Wiley & Sons, New York, 1989.